


**RESEARCH ARTICLE**

10.1029/2023MS003643

**Key Points:**

- The fetch is reduced after applying momentum perturbation and the reduction is directly proportional to the amplitude of the perturbations
- Applying momentum perturbation up to half the boundary layer height produces an adequate amount of turbulence without additional entrainment
- Momentum perturbations result in turbulent kinetic energy budget terms of higher magnitude than simulations without perturbations

**Supporting Information:**

Supporting Information may be found in the online version of this article.

**Correspondence to:**

M. Kumar,  
mukeshk@uci.edu

**Citation:**

Kumar, M., Jonko, A., Lassman, W., Mirocha, J. D., Kosović, B., & Banerjee, T. (2024). Impact of momentum perturbation on convective boundary layer turbulence. *Journal of Advances in Modeling Earth Systems*, 16, e2023MS003643. <https://doi.org/10.1029/2023MS003643>

Received 24 FEB 2023

Accepted 8 JAN 2024

**Author Contributions:**

**Conceptualization:** Mukesh Kumar, Alex Jonko, Tirtha Banerjee

**Data curation:** Mukesh Kumar

**Formal analysis:** Mukesh Kumar

**Funding acquisition:** Tirtha Banerjee

**Investigation:** Mukesh Kumar, Alex Jonko, William Lassman, Jeffrey D. Mirocha, Branko Kosović, Tirtha Banerjee

**Methodology:** Mukesh Kumar, Alex Jonko, Tirtha Banerjee

© 2024 The Authors. *Journal of Advances in Modeling Earth Systems* published by Wiley Periodicals LLC on behalf of American Geophysical Union.

This is an open access article under the terms of the [Creative Commons Attribution-NonCommercial-NoDerivs License](#), which permits use and distribution in any medium, provided the original work is properly cited, the use is non-commercial and no modifications or adaptations are made.

## Impact of Momentum Perturbation on Convective Boundary Layer Turbulence

Mukesh Kumar<sup>1,2</sup> , Alex Jonko<sup>1</sup> , William Lassman<sup>3</sup> , Jeffrey D. Mirocha<sup>3</sup>, Branko Kosović<sup>4</sup> , and Tirtha Banerjee<sup>2</sup> 

<sup>1</sup>Los Alamos National Laboratory, Los Alamos, NM, USA, <sup>2</sup>Department of Civil and Environmental Engineering, University of California, Irvine, Irvine, CA, USA, <sup>3</sup>Lawrence Livermore National Laboratory, Livermore, CA, USA, <sup>4</sup>National Center for Atmospheric Research, Boulder, CO, USA

**Abstract** Mesoscale-to-microscale coupling is an important tool for conducting turbulence-resolving multiscale simulations of realistic atmospheric flows, which are crucial for applications ranging from wind energy to wildfire spread studies. Different techniques are used to facilitate the development of realistic turbulence in the large-eddy simulation (LES) domain while minimizing computational cost. Here, we explore the impact of a simple and computationally efficient Stochastic Cell Perturbation method using momentum perturbation (SCPM-M) to accelerate turbulence generation in boundary-coupled LES simulations using the Weather Research and Forecasting model. We simulate a convective boundary layer (CBL) to characterize the production and dissipation of turbulent kinetic energy (TKE) and the variation of TKE budget terms. Furthermore, we evaluate the impact of applying momentum perturbations of three magnitudes below, up to, and above the CBL on the TKE budget terms. Momentum perturbations greatly reduce the fetch associated with turbulence generation. When applied to half the vertical extent of the boundary layer, momentum perturbations produce an adequate amount of turbulence. However, when applied above the CBL, additional structures are generated at the top of the CBL, near the inversion layer. The magnitudes of the TKE budgets produced by SCPM-M when applied at varying heights and with different perturbation amplitudes are always higher near the surface and inversion layer than those produced by No-SCPM, as are their contributions to the TKE. This study provides a better understanding of how SCPM-M reduces computational costs and how different budget terms contribute to TKE in a boundary-coupled LES simulation.

**Plain Language Summary** Grid nesting is a technique in atmospheric modeling where smaller model domains with finer resolutions are embedded in larger domains with coarser resolutions, allowing us to simulate processes for which a range of resolutions is important. When nesting a micro-scale domain, which resolves atmospheric turbulence, within a mesoscale domain, where turbulence is parameterized instead, the micro-scale domain needs to generate turbulence. This can take a long distance, reducing the area within the micro-scale domain where turbulence is fully developed. Turbulence generation methods can speed up this process, leading to more efficient multi-scale simulations. Here, we take a close look at one such turbulence generation method, which applies random perturbations to the momentum field along the boundaries of the micro-scale domain. We test several different configurations of momentum perturbations and evaluate their impacts on the turbulent kinetic energy budget within the micro-scale domain. Our results can be used as guidance on how to apply momentum perturbations most efficiently in grid-nested simulations.

### 1. Introduction

Grid nesting for mesoscale-to-large-eddy simulation (LES) is a useful technique for a variety of atmospheric model applications, from wind energy to wildfire spread investigations (Ching et al., 2014; Connolly et al., 2021; Haupt, Berg, et al., 2019; Haupt, Kosović, et al., 2019; Haupt et al., 2020; Mazzaro et al., 2019; Mirocha et al., 2014; Rai, Berg, Pekour, et al., 2017). In LES, realistic atmospheric turbulence emerges as a result of wind shear and buoyant forcing. However, realistic turbulence can require a long distance to develop. Turbulence generation methods can accelerate the generation of turbulence in the LES domain, effectively reducing the distance it takes for turbulent motions to develop, known as fetch. A common approach is to use a periodic domain where wind through the outflow boundary is recycled through the inflow boundary, retaining memory of the flow characteristics. However, periodic simulations are limited in their ability to represent heterogeneous surfaces or flow around obstacles. For these applications, a boundary-coupled simulation with an inflow and outflow is

**Project administration:** Mukesh Kumar, Alex Jonko, Tirtha Banerjee

**Resources:** Mukesh Kumar, Alex Jonko

**Software:** Mukesh Kumar, Jeffrey D. Mirocha

**Supervision:** Alex Jonko, Tirtha Banerjee

**Validation:** Mukesh Kumar

**Visualization:** Mukesh Kumar, Alex Jonko

**Writing – original draft:** Mukesh Kumar

**Writing – review & editing:**

Mukesh Kumar, Alex Jonko, William Lassman, Jeffrey D. Mirocha, Branko Kosović, Tirtha Banerjee

required (Connolly et al., 2021; Jähn et al., 2016; Liu et al., 2011; Mazzaro et al., 2017, 2019; Mirocha et al., 2014; Muñoz-Esparza et al., 2015, 2017; Rai, Berg, Kosović, et al., 2017; Talbot et al., 2012; Zhou & Chow, 2013). In boundary-coupled simulations using inflow data that does not contain resolved turbulence at the time and space scales of the LES discretization (e.g., from a mesoscale simulation), the development of resolved-scale turbulence generally requires a long fetch. Therefore, a large LES domain is needed (Mazzaro et al., 2017, 2019; Mirocha et al., 2014; Muñoz-Esparza, Kosović, García-Sánchez, & van Beeck, 2014; Muñoz-Esparza, Kosović, Mirocha, & van Beeck, 2014; Tabor & Baba-Ahmadi, 2010; Zajaczkowski et al., 2011) to capture the development of turbulence at fine scales, increasing computational cost (Connolly et al., 2021; Giani et al., 2022; Kumar et al., 2024; Mazzaro et al., 2017, 2019; Mirocha et al., 2010, 2014; Muñoz-Esparza, Kosović, Mirocha, & van Beeck, 2014). Incorporating adequate representation of turbulence within the model is also advantageous in understanding the role of fire-induced turbulence in wildfire behavior particularly in the wildland-urban interface (dos Santos & Yaghoobian, 2023; Kumar, 2022; Kumar et al., 2022). The concept of “time” is used to clarify the time that a parcel of air entering the inflow boundary experiences. One way to reduce the fetch is to run a precursor LES using periodic lateral boundary conditions with the same time and space discretization as the target LES and use the solution as inflow (Deardorff, 1972, 1980; Moeng & Sullivan, 1994; Moeng & Wyngaard, 1984; Muñoz-Esparza et al., 2016; Sauer et al., 2016; Smith & Skillingstad, 2009). However, the precursor simulation can require significant additional computational overhead, while also requiring forcing and surface conditions amenable to periodicity.

To overcome these challenges, a class of methods exists to initialize inflow boundary conditions with turbulence. For example, synthetic turbulence methods (Le et al., 1997; Pamiès et al., 2009) use digital filtering techniques of flow to infer Reynolds Stresses (Di Mare et al., 2006; Klein et al., 2003; Xie & Castro, 2008). These techniques require some information about the turbulence, either from observations or a periodic simulation. These methods also require relatively long fetches for the generation of turbulence. Another technique is the forcing method (Keat et al., 2004; Spille-Kohoff & Kaltenbach, 2001; Zajaczkowski et al., 2011), which uses wall-normal forces to move the flow into the domain inlet and generate the necessary Reynolds shear stress. However, it also needs a priori information about the targeted level of turbulence. Additional simulations are needed to generate an adequate amount of turbulence from this method in order to get a value that is closer to the observation.

As a compromise to using a turbulent inflow condition, another approach is to seed the inflow characteristics with added perturbations and allow the flow to develop realistic turbulence over a reduced fetch. One such method, the cell perturbation Method (CPM) (Muñoz-Esparza & Kosović, 2018; Muñoz-Esparza et al., 2015; Muñoz-Esparza, Kosović, Mirocha, et al., 2014), is a turbulence generation technique that employs random perturbations to potential temperature to induce small-scale motions near nested domain inflow boundaries. Mazzaro et al. (2019) modified the CPM approach by applying force perturbations to the momentum in the horizontal and vertical directions rather than perturbing the potential temperature fields. Mirocha et al. (2014) applied tendencies with sinusoidal amplitudes to temperature and velocity fields near inflow boundaries. This perturbation method produced promising results with the target turbulence level by triggering turbulent motions near the nested domain inflow boundaries. Muñoz-Esparza, Kosović, Mirocha, and van Beeck, 2014, Muñoz-Esparza et al. (2015), and Muñoz-Esparza and Kosović (2018) advanced this method by adding random forces instead of using sinusoidal perturbations, and also introduced perturbation cells. Perturbation cells are a span of contiguous model grid points located adjacent to the LES inflow boundaries that are perturbed with the same random value. A configuration of three cells consisting of eight grid points per cell in each of the horizontal directions is found to be optimal (Muñoz-Esparza, Kosović, Mirocha, & van Beeck, 2014). In addition, Muñoz-Esparza and Kosović (2018) optimized the CPM for different stability conditions. Thermal perturbations are chosen to encourage the most rapid formation of realistic correlations associated with buoyancy forces generated by the patches of resolved temperature variability. Although this optimization reduces the fetch size considerably relative to simulations using no perturbations, a nontrivial fetch still remains.

To further reduce the fetch required for turbulence generation, Mazzaro et al. (2019) applied tendencies directly to the momentum components, rather than potential temperature. This study showed that simulation perturbations that were applied to the vertical momentum term produced the shortest fetches overall, thereby further reducing fetch requirements and associated computational costs. However, the consequence of introducing momentum perturbations at the domain boundary on the fate and transport of turbulence in the domain is not yet well understood (Mazzaro et al., 2019). Quantifying the TKE budget in the Weather Research and Forecasting (WRF) LES domain can shed light on this question. In this study, we examine how momentum perturbations shift the

balance between the terms of the TKE budget in the convective boundary layer (CBL). We apply random (stochastically selected from within an amplitude range of 1,000 to 10,000  $\text{kg s}^{-4}$ ) forces in both vertical and horizontal directions (Kumar et al., 2021) and vary the vertical extent of the perturbations from 307 m (halfway between the surface and boundary layer and 1,608 m (top of the domain). TKE budget terms, including buoyant production, shear production, turbulent transport, and pressure correlation are then compared between simulations including these different perturbation configurations, periodic simulations, and simulations not including perturbations.

The goals of this study are as follows: (a) to explore the impact of a simple and computationally efficient Stochastic Cell Perturbation method (SCPM) to accelerate the generation of turbulence; (b) to understand how momentum perturbations shift the balance between the terms of the TKE budget; (c) to evaluate the role of momentum perturbation amplitudes on the TKE budget; and (d) to examine the effect of height in a CBL at which momentum perturbations are applied. We use the WRF LES model to simulate the CBL. Our results will advance the understanding of optimal strategies for performing coupled mesoscale-microscale simulations of atmospheric boundary layer processes.

This study is organized into three main sections. The methods and experimental set-up that are used to perform the SCPM using momentum perturbations (SCPM-M) are presented in Section 2. Section 3 describes the results and discussion of our analysis. Conclusions are presented in Section 4.

## 2. Methods

### 2.1. Model Configuration

In this study, we examine the impacts of applying SCPM-M in a convective (unstable) atmospheric boundary layer on the TKE budget. We use the WRF model version 4.1.3 (Skamarock et al., 2019) to conduct idealized LES simulations of a CBL based on measurements at the Scaled Wind Farm Technology (SWIFT) facility. The SWIFT site is located in west Texas's southern Great Plains and features nearly uniform terrain elevation covered with grass and small bushes. The site contains a 200 m meteorological tower that provides fast-response velocity and temperature data at 10 heights between 0.9 and 200 m from which mean and turbulence quantities could be computed.

To conduct our analysis of the SCPM-M method, we utilized an idealized nested LES setup with forcing that approximated the observed flow conditions occurring during a two-hour period during the afternoon of 8 November 2013, 18–20 Z. We used a two-domain nested configuration for which periodic lateral boundary conditions were applied on the outer domain, and the inner domain received lateral boundary data from the bounding domain solution. The goal of the setup was to closely approximate the observed mean wind speed and atmospheric stability observed during the case study period on the outer domain. We could then examine the representation of turbulence on the inner domain and also assess the efficacy of the perturbations to accelerate the formation and fidelity of the turbulence, relative to observed values.

Since the terrain was negligible, we approximated the surface as flat, with a uniform roughness length of 0.03 m. A very close agreement between the simulated and observed wind speeds across the depth of the tower was then produced by using a constant geostrophic forcing of  $(u_g, v_g) = (15.331, -9.431) \text{ ms}^{-1}$ , and a surface sensible heat flux of  $175 \text{ W/m}^2$ , which approximated the mean observed values from the lowest sensor height on the tower (0.9 m). These values ensured that the simulated wind direction aligned with the  $x$ -direction, allowing for the use of a nested domain elongated in the mean flow direction to facilitate the examination of the developing turbulence.

Simulations were initiated using a constant potential temperature between the surface and 250 m, with a capping inversion of 288 K/m applied up to the model top of approximately 1,600 m. The simulations were run for 6 hr with the first four used for spin-up, and the latter two used for examination. The WRF domains used horizontal grid resolutions of 240 and 12 m where the inner LES domain is one-way nested within an idealized mesoscale domain. Here, the effective WRF grid resolution ( $1,440 \text{ m} = 6 \times 240 \text{ m}$ ) is larger than the CBL height (600 m) and therefore the inflow conditions would not contain any resolved turbulence. The mesoscale domain (d01) has a horizontal extent of 115 km by 115 km, with 480 grid cells in both  $X$  and  $Y$  directions, while the LES domain (d02) has 961 grid cells in  $X$  direction and 481 grids in  $Y$  for a domain size of 11.5 km by 5.7 km. We use 88 vertical eta levels with the top level at 1,608 m (ztop). The minimum and maximum vertical grid spacing are 2.0032 m and 1606.5122 m respectively. An input sounding is used from the SWIFT facility with a capping inversion at

**Table 1**

The Table Shows a List of Simulations Performed in This Study Using Different  $K_{top}$  Values As Well As the Maximum Amplitude of Perturbations in Both Horizontal and Vertical Directions

Label	Amplitude $F_{xy}$ ( $\text{kgs}^{-4}$ )	Amplitude $F_z$ ( $\text{kgs}^{-4}$ )	$K_{top}$ (value)	Height (meters)
No-SCPM	—	—	—	—
Periodic	—	—	—	—
$K_{top}34L$	1,000	1,500	34	307
$K_{top}54L$	1,000	1,500	54	609
$K_{top}88L$	1,000	1,500	88	1,607
$K_{top}88M$	2,000	4,000	88	1,607
$K_{top}34H$	5,000	10,000	34	307
$K_{top}54H$	5,000	10,000	54	609
$K_{top}88H$	5,000	10,000	88	1,607

*Note.* It also shows the periodic and No-SCPM simulations used to compare the results of the SCPM-M cases.

approximately 600 m. The time step for integration is 0.5 s for the mesoscale domain and the outputs for the LES domain are stored every minute. We use a parent time step ratio of 50 and a resulting LES time step of 0.01 s. The general information on the model configuration is summarized in Table 2. Overall we perform nine WRF-LES simulations. The perturbation amplitudes chosen here are based on the work of Mazzaro et al. (2019), from which we selected a combination of all perturbation amplitudes, including the maximum amplitude, where each of these amplitudes is chosen at random from a uniform distribution (Mazzaro et al., 2019) that is defined by the largest perturbation value ( $F_{xy} = 5,000 \text{ kgs}^{-4}$  and  $F_z = 10,000 \text{ kgs}^{-4}$ ). The conversion of force perturbation amplitude into equivalent acceleration is nonlinear because the WRF transport equations are dependent on the mass in the system (Mazzaro et al., 2019). The acceleration that results from an individual force disturbance is inversely proportional to the pressure that the atmospheric column is exerting above the affected region. Instead of simply changing the individual velocity components, we take a novel technique (SCPM-M) and change the scalar tendency of the components. The model's equations of motion are able to calculate variations in velocity because of the fluctuations we introduce in such a manner (Mazzaro et al., 2019). Seven WRF-LES simulations are performed using various permutations of perturbation height and magnitude. In addition, we also perform one simulation with no inflow perturbations (referred to as No-SCPM) and another simulation with periodic boundary conditions (referred to as periodic) for context. By using periodic boundary conditions, it is implicitly assumed that both the atmospheric fields and the underlying land usage are encountered periodically during the simulation (Mirocha et al., 2014; Zhong et al., 2021). These simulations are summarized in Table 1 and described in more detail in Section 2.2.

**Table 2**

The Table Shows the Weather Research and Forecasting Model Configuration and the Summary of General Information on the Domain Design Used in This Study

WRF parameters	Values
WRF version	V4.1.3
Duration of simulation	6 hr
Spin-up time	4 hr
Duration of SCPM-M	2 hr
Horizontal resolution	240 m (parent domain), 12 m (LES domain)
Vertical resolution	88 vertical eta levels
Grid spacing	480 × 480 (parent domain), 961 × 481 (LES domain)
Grid spacing (periodic)	600 × 600
Time step	0.5 s (parent domain), 0.01 s (LES domain)
Parent time step ratio	50

We use the YSU (Hong et al., 2006) PBL scheme for the mesoscale domain. We do not use cloud micro-physics, land surface, cumulus physics, or radiation physics in this study. We use the nonlinear backscatter and anisotropy (NBA) scheme (Kosović, 1997; Mirocha et al., 2010) to model subgrid-scale (SGS) mixing in the LES and mesoscale domain respectively. In the LES sub-domain, the Monin-Obukhov Similarity Theory (MOST) is used to parameterize the surface layer (surface layer option 1 (Jiménez et al., 2012; Monin & Obukhov, 1954)).

## 2.2. Experimental Set-Up

### 2.2.1. SCPM Simulations

In this study, we apply momentum perturbations to  $8 \times 8 \times 1$  grid point cells from the surface up to the 34th, 54th, and 88th pressure levels along the inflow boundary of the LES domain (denoted as Ktop34, Ktop54, and Ktop88 respectively). The vertical extent of these perturbations is 307, 609, and 1,607 m, respectively. These extents correspond to heights halfway between the surface and the capping boundary layer, the height of the capping boundary layer, and the top of the domain. We also vary the perturbation amplitude. Simulations with low amplitude perturbations ( $F_{xy} = 1,000 \text{ kgs}^{-4}$ ;  $F_z = 1,500 \text{ kgs}^{-4}$ ) are denoted as Ktop34L, Ktop54L, and Ktop88L, and simulations with high amplitude perturbations ( $F_{xy} = 5,000 \text{ kgs}^{-4}$ ;  $F_z = 10,000 \text{ kgs}^{-4}$ ) as Ktop34H, Ktop54H, and Ktop88H (Table 1).

In addition, we would like to investigate whether forces lower than the higher amplitude perturbations are able to reduce the fetch in TKE generation. Therefore, we apply a combination of forces that have forcing amplitude between the higher and lower amplitude perturbations. We refer to these forces as medium amplitude perturbations. For medium amplitude perturbations ( $F_{xy} = 2,000 \text{ kgs}^{-4}$ ;  $F_z = 3,000 \text{ kgs}^{-4}$ ), we only perform a simulation for the Ktop88 case (denoted by Ktop88M in Table 1) for the following reason. This case involves the application of forces above the CBL height. This, in turn, gives us the opportunity to examine the impact of these forces throughout the entire inner domain, that is, both above and below the CBL height. In contrast, applying medium amplitude perturbations at other heights (as in the case of Ktop34 and Ktop54) is devoid of this opportunity.

### 2.2.2. No-SCPM and Periodic Simulations

In addition to the SCPM simulations described above, we also perform a simulation where no perturbations are applied, the No-SCPM simulation. The domain configuration and simulation time for this simulation are the same as for the SCPM-M simulations.

We also compare SCPM simulations against a simulation where turbulence is developed through the use of periodic boundary conditions, that is, output conditions at the outflow become input conditions at the inflow. We do not use nested domains for the periodic simulation. Rather, a single LES domain with 600 grid cells in  $X$  direction and 600 grids in  $Y$  is used. The domain size is 7.2 km by 7.2 km. We also use 88 vertical eta levels with the top level at 1,608 m (ztop). The input sounding remains the same as in SCPM-M simulations. The time step for integration is 0.05 s and the outputs for the LES domain are stored every minute. Both periodic and No-SCPM simulations are summarized in Table ref T1 SCPM M.

## 2.3. Analysis Methods

In order to calculate mean and turbulent statistics, we use standard turbulence decomposition, where  $u' = U - \bar{U}$ ,  $v' = V - \bar{V}$ ,  $w' = W - \bar{W}$ , and  $\theta' = \theta - \bar{\theta}$  where  $\bar{\theta}$ . Here  $U$ ,  $V$ , and  $W$  are the instantaneous velocity components,  $\theta$  is the potential temperature, over-bars denote time averaging, and primes denote fluctuations from the mean. We choose time averaging to evaluate the temporal behavior and variations of mean fields to calculate perturbations in these fields in our study. The purpose is to capture the average behavior of the fields over a certain time period by using temporal averaging and varying perturbations of the fields, which could potentially show interesting patterns and trends. The wind speed is calculated as  $\sqrt{\bar{U}^2 + \bar{V}^2}$  with an averaging time of the last 30 min of simulation that is, from 19:30 Z to 20 Z UTC (1:30–2 p.m. Central time). The heat flux is given by  $\bar{w'}\bar{\theta'}$  and momentum flux is given by  $\bar{w'}\bar{u'}$ .

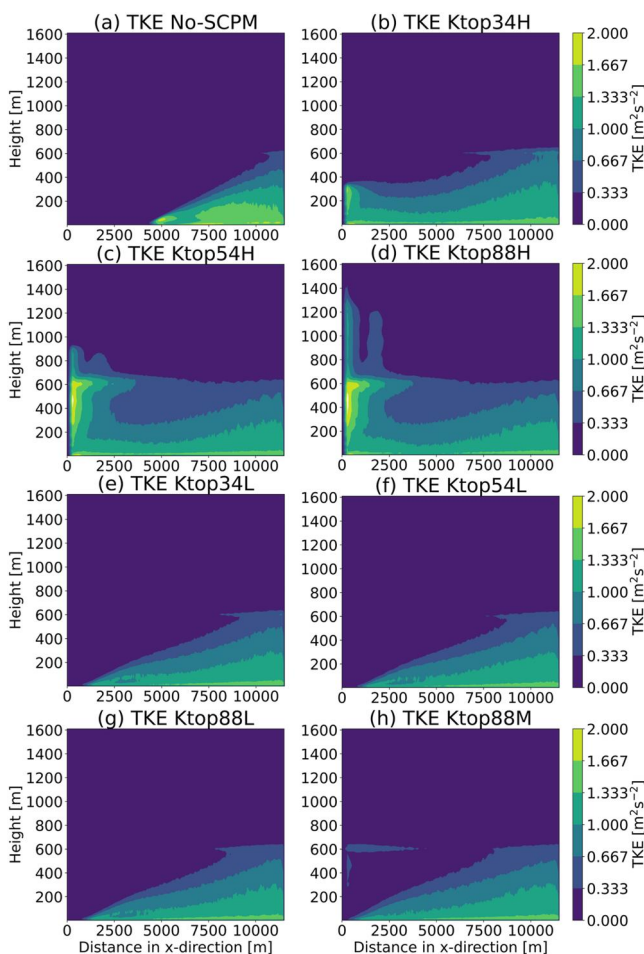


**Figure 1.**  $Y$ -averaged turbulent kinetic energy ( $\text{m}^2/\text{s}^2$ ), computed over the entire inner domain, compared between simulations with and without momentum perturbation with different perturbation amplitudes and vertical extents with panels (a) No-SCPM, (b) Ktop34H, (c) Ktop54H, (d) Ktop88H, (e) Ktop34L, (f) Ktop54L, (g) Ktop88L, and (h) Ktop88M as shown in Table 1.

at which turbulent fluctuations start to develop is called fetch (Mazzaro et al., 2017, 2019). We observe that for simulations without momentum perturbation (No-SCPM), turbulence begins to develop 5,000 m into the domain, with a significant fetch, and a realistic representation of fully developed turbulent structures only appears in the last 25% of the domain. After applying SCPM-M, the fetch is reduced significantly for all perturbed cases.

For high amplitude perturbations (Figures 1b–1d), the fetch is diminished, but the maximum of TKE is present along the inflow boundary and near the boundary layer top. For Ktop54H and Ktop88H, positive values of TKE extend above the boundary layer, an artifact related to the high perturbation height and amplitude (Figures 1c and 1d). Furthermore, for Ktop34H, the TKE maximum is present near the bottom of the domain, near the surface and most importantly, the fetch has reduced significantly (Figure 1b).

In the case of lower and medium amplitude perturbations (Figures 1e–1h), the TKE maxima near the boundary layer are not present. We also observe that the rate at which the TKE increases with the downwind  $x$  direction is similar for the medium and lower amplitude perturbations but not the same as the No-SCPM case (Figure 1a).

These spatial patterns highlight that the vertical and horizontal extent of inflow perturbations can influence the underlying turbulence evolution. Moreover, SCPM-M produces a vertical profile of TKE that spans the boundary layer more rapidly than without the perturbations. In addition, tuning the amplitude of the

The  $\bar{e}$  is the TKE, defined as:

$$\bar{e} = 0.5(\bar{u}'\bar{u}' + \bar{v}'\bar{v}' + \bar{w}'\bar{w}')$$
 (1)

The TKE budget equation is given by Stull (1988):

$$\frac{\partial \bar{e}}{\partial t} + \bar{U}_j \frac{\partial \bar{e}}{\partial x_j} = \delta_{i3} \frac{g}{\theta_v} \bar{u}_i' \bar{\theta}_v' - \bar{u}_i' \bar{\theta}_j' \frac{\partial \bar{U}_i}{\partial x_j} - \frac{1}{\bar{\rho}} \frac{\partial \bar{u}_j' p'}{\partial x_i} - \epsilon$$
 (2)

The first and second terms on the left-hand side of Equation 2 represent local storage or the tendency of TKE and the advection of TKE by mean wind, respectively. The terms on the right-hand side of Equation 2 in order from left to right represent the buoyant production or consumption term, a mechanical or shear production term, the turbulent transport of TKE, a pressure correlation term, and the viscous dissipation of TKE, respectively (Stull, 1988).

The TKE budget equation after assuming horizontal homogeneity, neglecting subsidence, and choosing a coordinate system that is in the direction of mean wind, is simplified as:

$$\frac{\partial \bar{e}}{\partial t} = + \frac{g}{\theta_v} \bar{w}' \bar{\theta}_v' - \bar{u}' \bar{w}' \frac{\partial \bar{U}}{\partial z} - \frac{\partial \bar{w}' e}{\partial z} - \frac{1}{\bar{\rho}} \frac{\partial \bar{w}' p'}{\partial z} - \epsilon$$
 (3)

Using these concepts and equations, we compute TKE, heat, and momentum fluxes, as well as TKE budget terms associated with buoyancy, shear, transport, and pressure correlation for all simulations outlined in Table 1. In the next section, we present and discuss the results of this analysis.

## 3. Results and Discussion

### 3.1. TKE

#### 3.1.1. Spatial Variation of TKE

TKE is a measure of the intensity of turbulence. We calculate TKE for all simulations (Table 1) and compare its variation over height ( $z$ ) and streamwise distance ( $x$ ) (Figure 1). The distance from the inflow boundary

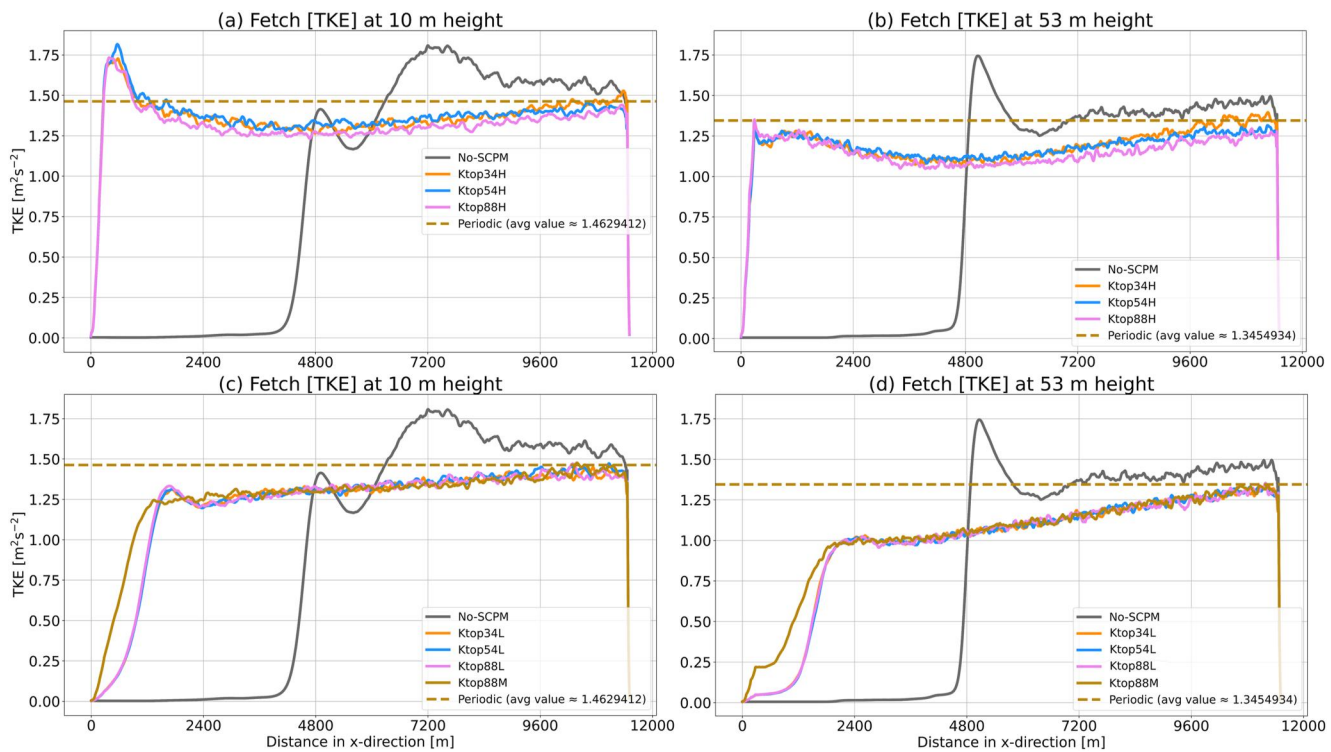


**Figure 2.** Fetch of  $Y$ -averaged turbulent kinetic energy (TKE) ( $\text{m}^2/\text{s}^2$ ), computed after applying momentum perturbation with higher, medium, and lower amplitudes as shown in (Table 1) and show fetch at (a) 10 m height for periodic, No-SCPM, and higher amplitude SCPM-M, (b) 53 m height for periodic, No-SCPM, and higher amplitude SCPM-M, (c) 10 m height for periodic, No-SCPM, and lower and medium amplitude SCPM-M, (d) 53 m height for periodic, No-SCPM, and lower and medium amplitude SCPM-M. These plots are generated for TKE that are  $Y$ -averaged over the entire inner domain.

perturbation helps minimize the fetch to fully develop the TKE. Here, the term “fully developed” does not mean that TKE has reached the exact same value, but rather the same order of magnitude. However, if the height of perturbations approaches or exceeds the boundary layer, this leads to artifacts in the flow field above the boundary layer height.

### 3.1.2. Fetch

In boundary-coupled simulations using inflow data that does not contain resolved turbulence at the time and space scales of the LES discretization (e.g., from a mesoscale simulation), the development of resolved-scale turbulence generally requires a long fetch. We compare the variation of  $Y$ -averaged TKE over height and longitude in the  $y$  and  $x$  axes respectively (at two heights, 10 m, and 53 m, Figure 2) from the perturbed cases and the periodic simulation to investigate the extent of the fetch. The distance from the inflow boundary at which the TKE from the SCPM-M simulations becomes comparable to the TKE obtained from the periodic simulation can be used as a rough estimator for the fetch. The fetch required to fully develop turbulence is referred to as “required fetch” hereafter.

We observe that the required fetch is longest for the No-SCPM simulation (Figure 2a). At 10 m height, the required fetch for the No-SCPM case is around 9,000 m, and at 53 m the fetch is around 7,200 m (Figures 2a–2d). Before the fetch is fully established, the TKE increases to an unrealistically high level as indicated by the large departure from the periodic case.

However, after applying SCPM-M, the required fetch is reduced significantly. At both 10 and 53 m, the TKE is fully developed around 2,000 m for all perturbed cases as shown in Figure 2. Quantitatively, we find that the TKE reaches 80% of its steady-state magnitude at 2,000 m from the inlet boundary in the case of SCPM-M simulations when compared to the periodic simulation (Figure 2). On the other hand, the No-SCPM scenario takes 5,000 m to achieve the same level of TKE. At the last quarter of the domain, starting at  $x = 9,600$  m, the TKE for the perturbed cases is quite close to the periodic case. Therefore, we will use the last three-quarters of the domain

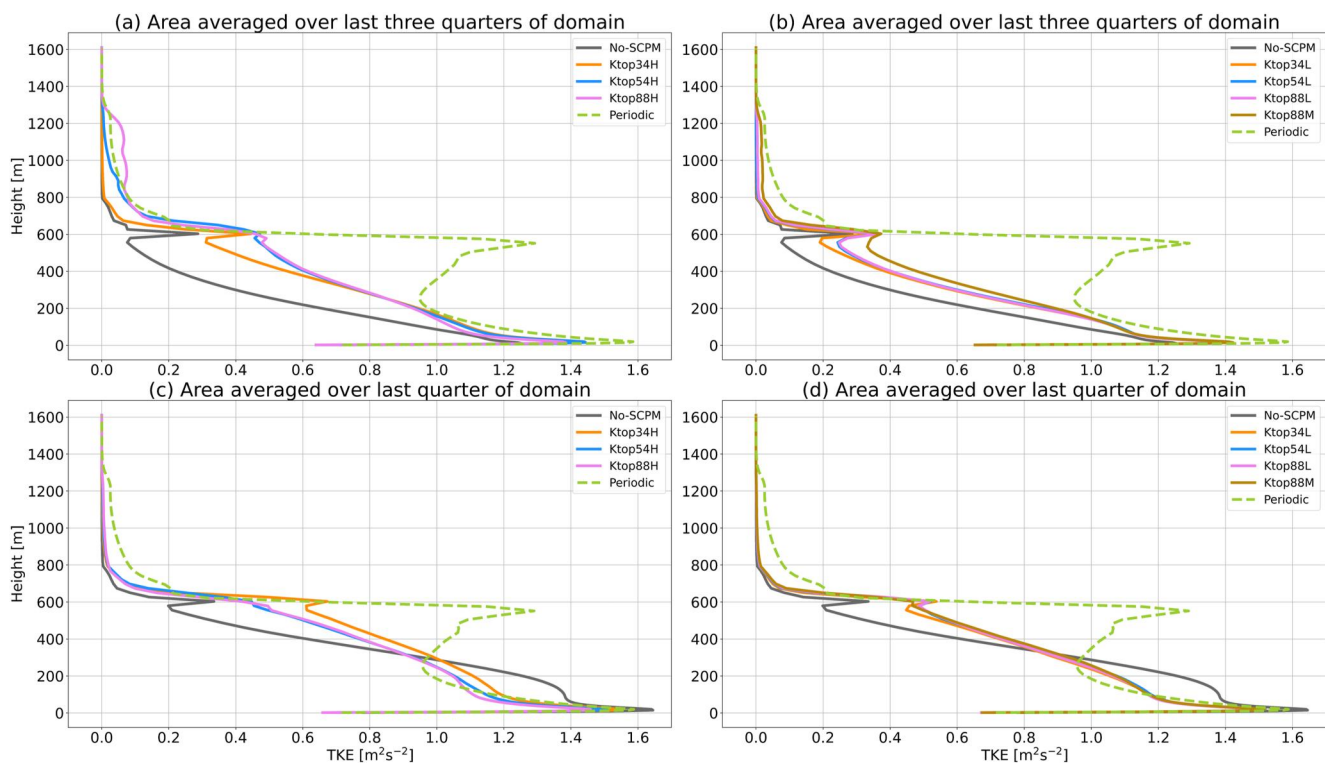


**Figure 3.** Area-averaged turbulent kinetic energy (TKE) ( $\text{m}^2/\text{s}^2$ ) profiles, computed for the inner domain after applying momentum perturbation with higher amplitude (Table 1) in the right panels and lower and medium amplitudes (Table 1) in the left panels, respectively. Profiles (a) and (b) show TKE values that are area-averaged over the last three-quarters of the domain, that is, overall  $y$  and  $x$  from 2,880 m to 11,520 m for (a) Periodic, No-SCPM, and high amplitude SCPM-M (Ktop34H, Ktop54H, and Ktop88H); (b) Periodic, No-SCPM, and low and medium amplitude SCPM-M (Ktop34L, Ktop54L, Ktop88L, and Ktop88M). While, panels (c) Periodic, No-SCPM, and high amplitude SCPM-M (Ktop34H, Ktop54H, and Ktop88H), and (d) Periodic, No-SCPM, and low and medium amplitude SCPM-M (Ktop34L, Ktop54L, Ktop88L, and Ktop88M) are the TKE profiles that are area-averaged over only the last quarter of the domain, that is, overall  $y$  and  $x$  from 86,400 to 11,520 m.

( $x$  from 2,880 m to 11,520 m) to average over turbulence statistics subsequently reported in this study. The TKE profiles averaged over the last quarter of the domain ( $x$  from 86,400 m to 11,520 m) will be reported only for reference in Section 3.1.3. Furthermore, the TKE evolves over time and space after applying SCPM-M. For instance, we can see this spatial evolution when we compare the area-averaged TKE over the last quarter of the domain to the area average over the last three-quarters of the domain. The former is much closer to the periodic value than the latter. For more information on the effects of the spatial averaging domain on fluxes and TKE budget terms, please see Supporting Information S1.

### 3.1.3. TKE Profiles

Based on the discussion in the previous Section 3.1.2, we compare the TKE profiles that are averaged over two different areas: three-quarters of the domain (overall  $y$  and  $x$  from 2,880 m to 11,520 m) farthest away from the inflow (Figures 3a and 3b), and last quarter of the domain (overall  $y$  and  $x$  from 86,400 m to 11,520 m) farthest from the inflow (Figures 3c and 3d). We observe that applying SCPM-M produces TKE closer to the periodic case regardless of the extent of its application (Figures 3a–3d).

As it is observed in Figure 3, the TKE is highest near the surface and decreases with height in all SCPM-M simulations and as well as in the case of No-SCPM. Up to 200 m, the TKE is similar for all the perturbed cases as well as the periodic case, while the TKE for the No-SCPM case is lower, when the TKE is area-averaged over the last three-quarters of the domain (Figures 3a and 3b). However, between 300 m and up to the CBL height, SCPM-M cases with higher amplitudes (Ktop34H, Ktop54H, and Ktop88H) are closer to the periodic case; while No-SCPM shows the largest deviation from the periodic case (Figures 3a and 3b). When the last quarter area-averaged profiles are compared (Figures 3c and 3d), we find that the TKE is highest for the No-SCPM case below 300 m and it decreases sharply above 300 m, deviating the most from the periodic case. However, the

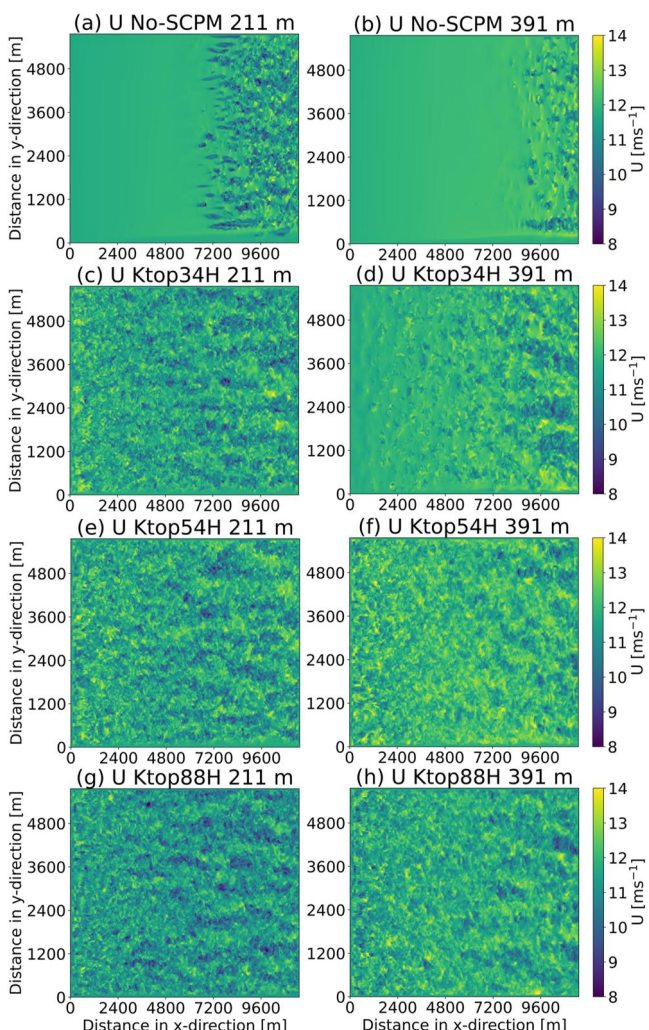


**Figure 4.** Instantaneous  $U$  component of velocities ( $\text{ms}^{-1}$ ), computed at two different heights that are at half (level = 27,  $z = 211 \text{ m}$ ) and at two-thirds (level = 37,  $z = 391 \text{ m}$ ) of the boundary layer height for (a and b) No-SCPM, (c and d), Ktop54H, (e and f) Ktop54H, and (g and h) Ktop88H. The color bar corresponds to the magnitude of velocity for panels (a–h).

higher as compared to the other perturbed cases. Between 100 and 500 m, the lowest wind speed is observed for the periodic simulation (dashed line) followed by the Ktop88H case (purple line) in Figures 5a and 5b, compared to the other cases. Wind speed profiles for the lower and medium SCPM-M cases are similar to each other but lower than the No-SCPM case up to about 500 m. We evaluated the model's capacity to accurately represent the atmospheric conditions and it enhanced our confidence in the results by comparing the model results with the tower data that is currently available in the form of observations from the SWIFT site. We compare the observational wind speed (Figure 7a) and potential temperature (Figure 7b) profiles with model results at three different instances that is, 18, 19, and 20 Z. Figures 7a and 7b shows reasonable agreement between the sounding and model wind speed and very good agreement for potential temperature respectively, for the lower 200 m of the atmosphere for all three times.

### 3.2.3. Velocity Variance Statistics

In order to examine the contributions of the velocity variance components ( $\sigma_u^2$ ,  $\sigma_v^2$ ,  $\sigma_w^2$ ) to the TKE, we area-average them over the last three-quarters of the domain and compute in Figure 6. The notations with primes and overbars for variance are indicated with sigmas and subscripts. Similar to the TKE profiles in Figure 3, all

SCPM-M cases are closer to the periodic case for all heights. In addition, we also observe that the medium and lower amplitude SCPM-M cases are almost equal in magnitude throughout the domain (Figure 3d). From the high amplitude SCPM-M cases, the TKE for the Ktop34H is closest to the periodic case above 300 m (Figure 3c). It is important to note that the effect of momentum perturbation is not only to enhance TKE but rather to adjust TKE closer to the appropriate levels at all heights within the CBL. Therefore, even though SCPM-M is shown to correct less than half the bias while TKE is evolving, measured as the difference in TKE values between the periodic simulation and the No-SCPM simulation, for a significant portion of the CBL, it performs better than No-SCPM for a significant portion of the CBL.

## 3.2. Mean and Instantaneous Flow Features

### 3.2.1. Instantaneous Flow Features

Figure 4 shows the instantaneous  $U$  component of velocity at two-thirds and half of the CBL height (211 and 391 m, respectively) for simulations without SCPM and the SCPM applied to three different vertical extents. These velocities are shown at the last instant of the simulation period that is, at 20 Z (UTC) for the nested LES domain. As observed in Figures 1–3, and in previous studies, such as Mazzaro et al. (2017, 2019), a large fetch is required for the No-SCPM simulation. The fetch is reduced significantly whenever perturbations are applied, regardless of the extent and amplitude of the applied momentum perturbation.

### 3.2.2. Mean Wind Speed Profiles

We find that the time and area-averaged (over the last 30 min of simulation for the last three-quarters of the domain) vertical profiles of the wind speed for the different simulation cases have a logarithmic profile near the surface layer up to the height of 200 m (Figure 5a). In this study, we are interested in the lower atmospheric boundary layer (200 m), focusing on applications such as wind energy. We used the term “surface layer” as 10%–20% of the boundary layer height. Under convective conditions, the profiles of mean velocity would not be perfectly logarithmic, but one can use MOST to obtain stability correction functions. However, in this case, since very mildly unstable conditions are used, we did not focus on stability corrections. The extent and amplitude of inflow perturbations have a small effect on the wind speed profiles. Between 100 and 500 m, the wind speed for the No-SCPM case is

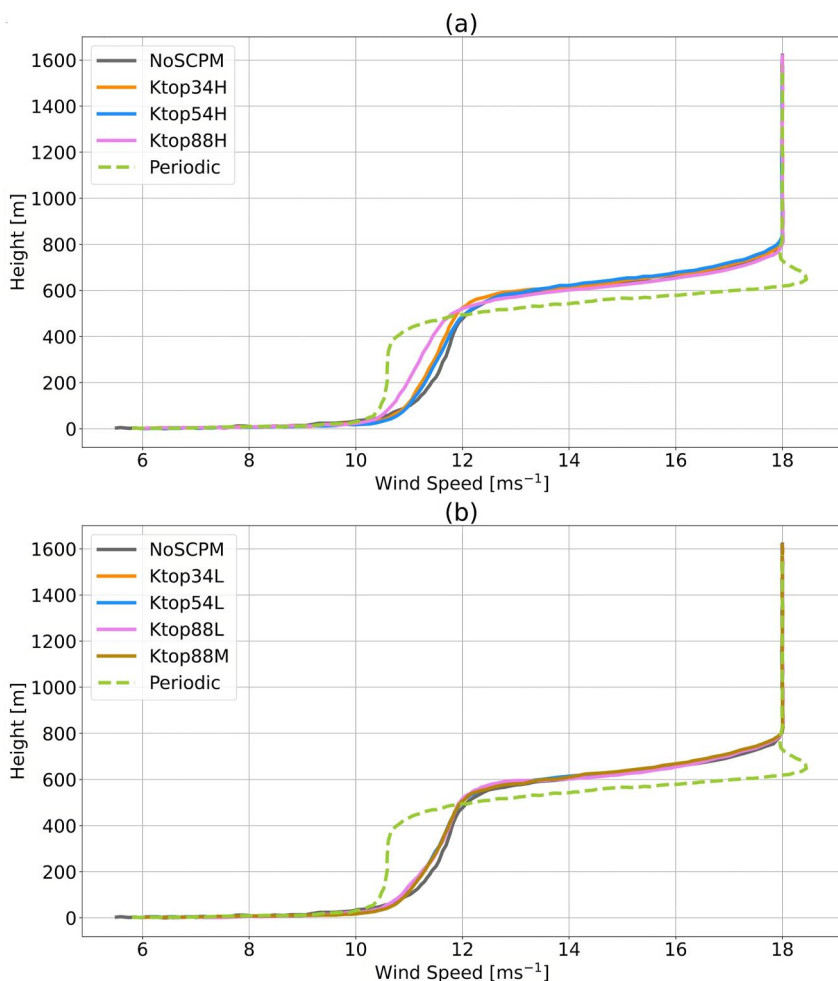


**Figure 5.** Wind speed ( $\text{ms}^{-1}$ ) area-averaged over three-quarters of the domain (all  $y$  and  $x$  from 2,880 m to 11,520 m) for all the cases as shown in Table 1 for (a) higher, (b) lower and medium amplitude SCPM-M as well as No-SCPM and periodic simulation. The wind speeds are generated from the last 30 min of the simulation time period that is, from 19 Z (UTC) to 20 Z (UTC) and for the top of the entire simulation inner domain up to 1,608 m.

three velocity variances are higher for the SCPM-M cases compared to the No-SCPM case. The  $\sigma_w^2$  is higher for the Ktop34H case around 200 m. Just below the CBL height of 600 m, the  $\sigma_u^2$  and  $\sigma_v^2$  are higher for Ktop88H compared to the other cases.

### 3.3. Fluxes of Sensible Heat and Momentum

Similar to the other turbulence statistics, the fluxes of sensible heat ( $\overline{w'\theta'}$ ) and momentum ( $\overline{u'w'}$ ) are averaged over the last three-quarters of the domain and plotted in Figure 8. We observe that below 200 m, the fluxes of sensible heat and momentum are higher for the No-SCPM case as compared to the SCPM-M cases (Figure 8). This could be attributed to unrealistically high levels of TKE in the No-SCPM case in the last two-quarters of the domain, as observed in Figure 2. Above 200 m, the sensible heat flux for the SCPM-M cases is similar to the No-SCPM case (Figures 8a and 8b). However, the momentum fluxes are higher for the SCPM-M cases than the No-SCPM (Figures 8c and 8d) case above 200 m.

Among the SCPM-M cases, the Ktop34H has a higher magnitude of sensible heat flux than the other cases (Figure 8a). The lower and medium amplitude SCPM-M cases are similar in the sensible heat flux throughout the domain (Figure 8b). For the momentum flux, all the high-amplitude SCPM-M cases (Figure 8c) and all the low and medium-amplitude cases (Figure 8d) are similar to each other.

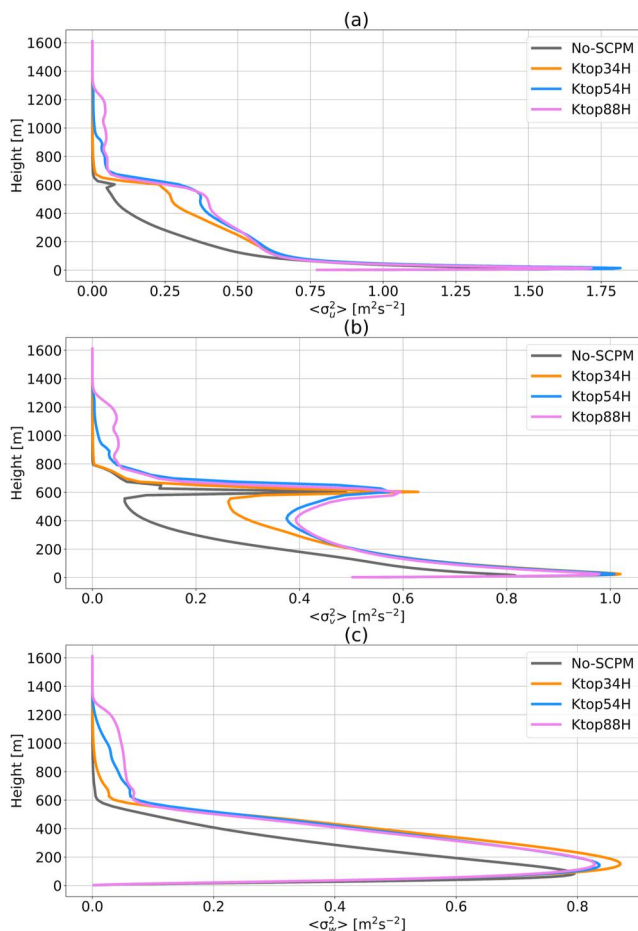


**Figure 6.** Area-averaged (a)  $\langle \sigma_u^2 \rangle$ , (b)  $\langle \sigma_v^2 \rangle$ , and (c)  $\langle \sigma_w^2 \rangle$  over three quarters of the domain (all  $y$  and  $x$  from 2,880 to 11,520 m) for No-SCPM, Ktop34H, Ktop54H, and Ktop88H. These results are shown from the last simulation period at 20 Z and for the top of the entire simulation inner domain up to 1,608 m. The angular brackets denote area averaging.

general, lower amplitude perturbations reduce the fetch and do not create additional entrainment. Another important point to note is that the application of momentum perturbation (SCPM-M) is sufficient to modify the buoyancy term, without requiring perturbing the temperature field, as demonstrated by Mazzaro et al. (2019). This could be explained by the fact that the force-perturbation method generates additional  $w'$  fluctuations in the turbulent field, which excites the vertical sensible heat flux  $\overline{w'\theta'}$  as well.

As observed in Figures 10a and 10b, the vertical profile of the buoyancy term follows the same trend of the sensible heat flux profiles as shown in Figures 8a and 8b.

### 3.4.2. Shear Term

The momentum flux  $\overline{u'w'}$  is negative as momentum is absorbed toward the ground, and therefore the term  $-\overline{u'w'}(\partial U/\partial z)$  is positive and a source of TKE. Without applying momentum perturbation, we find that WRF-LES is unable to generate shear production (Figure 9c) from the very beginning of the lateral boundary and thus results in a long fetch before turbulence develops, as observed in the plan-view plots of velocities (Figure 4 and Figure S1 in Supporting Information S1). Since applying SCPM-M reduces the fetch in velocity generation, in a similar fashion, the fetch in shear production is also reduced because it is a combination of both ( $u$  and  $w$ ) quantities  $(-\overline{u'w'}(\partial U/\partial z))$ .

At the top of the inversion layer, Ktop34H has the highest entrainment flux (this is where the “potentially” warmer air is entrained into the CBL), as indicated by the strongly negative sensible heat flux at the top of the CBL for Ktop34H. Ktop88H and Ktop54H simulations produce similar entrainment fluxes of heat from above into the CBL. This is due to turbulence being artificially excited near and above the top of the CBL.

### 3.4. TKE Budget

Since sensible heat flux and momentum flux contribute to TKE generation, the components of the budget equation for the TKE are worth investigating for the simulated cases. Therefore, individual terms of the TKE budget are discussed in this section. Figure 9 shows the  $y$ -averaged components of the TKE budget for the No-SCPM (left column) and the Ktop34H case (right column). We focus our discussion on the Ktop34H case because (a) additional entrainment at the capping inversion level is very low compared to the other cases and (b) the reduction in fetch is significant. The other high amplitude cases, while reducing the fetch, generate additional entrainment at the CBL height. In contrast, the low amplitude and medium amplitude cases are less efficient in the fetch reduction.

The  $y$ -averaged TKE budget terms for other SCPM-M cases are plotted in Figure S3 of Supporting Information S1. Vertical profiles of the TKE budget terms, averaged over the three quarters farthest from the inflow of the domain are shown in Figure 10 for all SCPM-M cases as well as the No-SCPM case.

#### 3.4.1. Buoyancy Term

The  $y$ -averaged buoyancy term  $(g/\theta)\overline{w'\theta'}$  for the No-SCPM and Ktop34H cases are plotted in Figures 9a and 9b.

We observe that for the No-SCPM case, the buoyancy term starts developing from the center of the  $x$ -axis (Figure 9a). However, the fetch for the buoyancy term is reduced significantly for the perturbed cases (Figure 9b and Figure S3 in Supporting Information S1). For Ktop54H and Ktop88H, the fetch is reduced appreciably, however, additional entrainment can be observed near the CBL height (Figures S3a and S3b in Supporting Information S1). In

the

As observed in Figures 10a and 10b, the vertical profile of the buoyancy term follows the same trend of the sensible heat flux profiles as shown in Figures 8a and 8b.

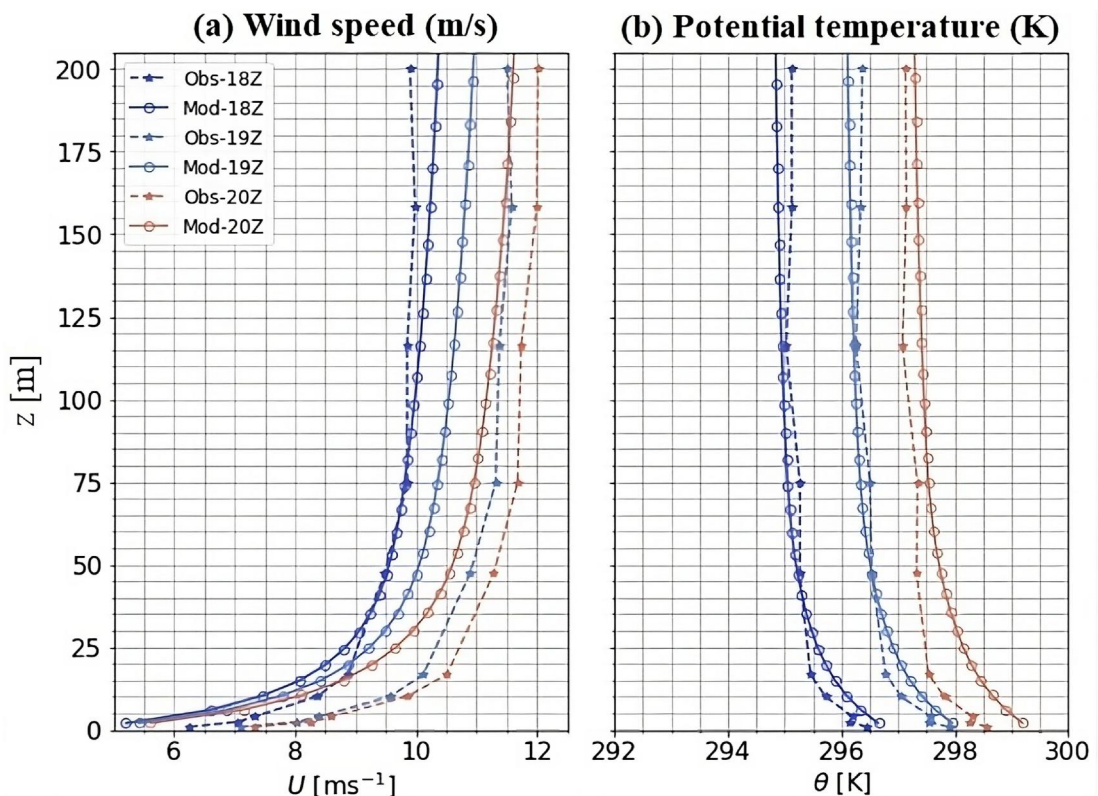


**Figure 7.** Profiles of domain-averaged (a) wind speed and (b) potential temperature at hours 18, 19, and 20 Z (UTC) during assessment (18–20 Z) periods, versus centered 30-min-averaged quantities observed at the Scaled Wind Farm Technology.

We find that SCPM-M with higher amplitudes reduces the fetch in shear production significantly, as shown in Figure 9d. However, in  $\text{Ktop54H}$  and  $\text{Ktop88H}$ , strong shear production is observed at the beginning of the LES domain near the lateral boundary (Figures S4a and S4b in Supporting Information S1). This can be attributed to the application of SCPM-M near and above the CBL, which produces superfluous turbulent motions and ultimately contributes to strong shear production above the CBL. Furthermore, we observe a small to moderate intensity of shear production near the CBL height for the SCPM-M cases due to a strong  $\partial U / \partial z$  in the last quarter of the domain (Figure 9d). Other SCPM-M cases are shown in Supporting Information S1. In other SCPM-M cases with lower and medium amplitudes (Figures S4c–S4f in Supporting Information S1), the fetch is reduced to a great extent without the generation of spurious motions near the lateral boundary at the beginning of the innermost domain.

Applying momentum perturbation within the LES domain contributes to maximum shear production near the surface in all the cases, as shown in Figures 10c and 10d. When compared to the No-SCPM case, the largest magnitude of shear production with SCPM-M is higher below the height of 200 m. There is a small but sharp jump in the shear term near the entrainment zone, regardless of the amplitudes of SCPM-M. Shear production reaches zero just above the CBL in all the SCPM-M cases. It diminishes completely at 650 m above the surface.

### 3.4.3. Turbulent Transport Term

In a planar homogeneous case without subsidence, the turbulent transport term in the TKE budget integrates over the domain height to null, indicating that TKE is transferred among horizontal planes (Stull, 1988). The  $\overline{w'e}$  is the major contributor to the turbulent transport term in the TKE budget equation. Here, we compare the  $y$ -averaged turbulent transport terms for different SCPM-M cases. Furthermore, the planar homogeneous assumption is on the boundary condition and land cover and it is not on the flow itself. In addition, even with the planar homogeneous flow boundary condition, the TKE needs space to develop.

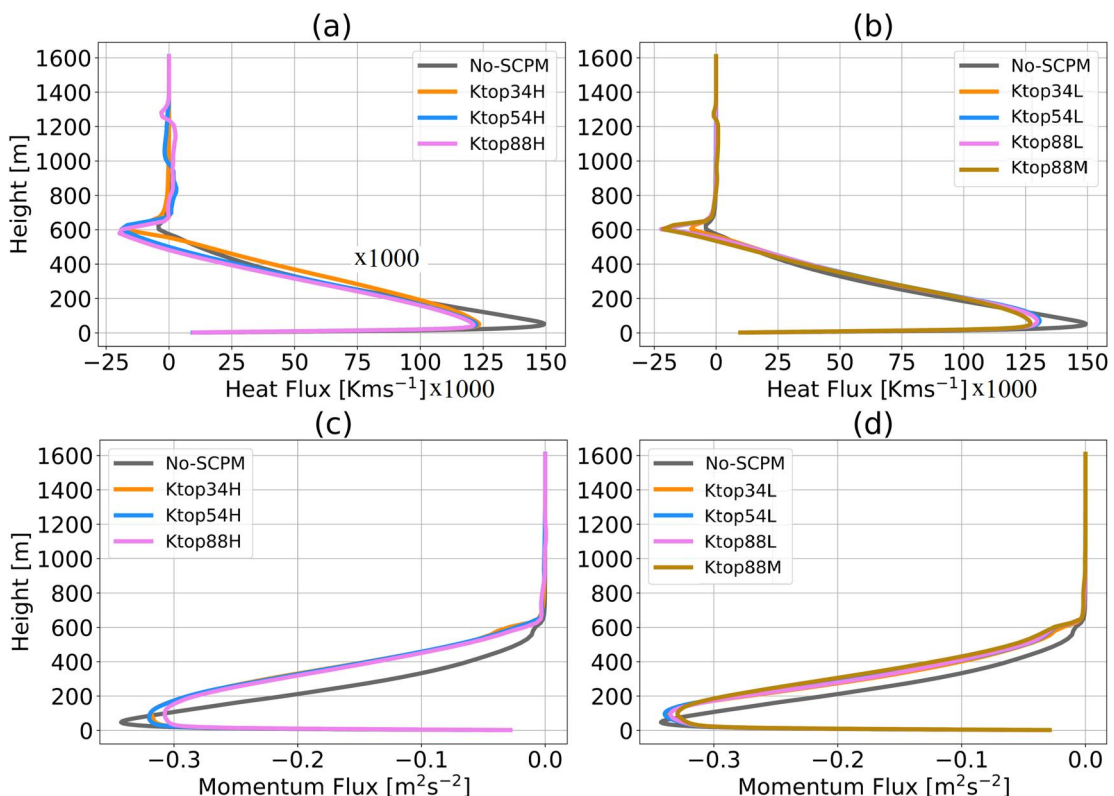


**Figure 8.** Heat flux ( $\bar{w}'\theta'$ ) profiles after applying momentum perturbation (SCPM-M) with (a) higher amplitudes of forces, as shown in (Table 1), (b) lower and medium amplitudes of forces; momentum flux ( $\bar{u}'w'$ ) with (c) higher amplitudes of forces, and (d) lower and medium amplitudes of forces. The heat flux values are in Km/s and are multiplied by 1000 for readability. In addition, these profiles are computed in a way that the heat flux ( $\bar{w}'\theta'$ ) and momentum flux ( $\bar{u}'w'$ ) are area-averaged over the last three-quarters of the inner domain that is, overall  $y$  and  $x$  from 2,880 to 11,520 m and are shown for the top of the entire simulation inner domain up to 1,608 m.

Beyond  $x = 4,800$  m, gain due to turbulent transport ( $T > 0$ ) alternates with loss due to turbulent transport ( $T < 0$ ), as we ascend along the  $y$ -axis up to the CBL height in the No-SCPM case (Figure 9e). After applying SCPM-M, redistribution of the TKE starts at the beginning of the domain, as shown in Figure 9f (Figures S5a–S5f in Supporting Information S1 shows all the other cases for the sake of completion). Therefore, the fetch in the generation of the turbulent transport term is reduced significantly with SCPM-M. However, the SCPM-M cases with higher amplitude produce more entrainment near the inflow boundary as compared to the lower amplitude SCPM-M cases (Figure 9f and Figures S5a–S5f in Supporting Information S1). Among the higher amplitude SCPM-M cases, Ktop34H produces lower entrainment (Figure 9f; Figures S5a and S5b in Supporting Information S1). The entrainment is not produced for the lower amplitude SCPM-M cases (Figures S5c–S5e in Supporting Information S1).

We also compute the profiles of the turbulent transport terms that are area-averaged over the last three-quarters of the domain (all  $y$  and  $x$  from 2,880 to 11,520 m) for the simulations in this section (Figures 10e–10f). We find that without the SCPM-M, the turbulent transport term increases up to 25 m and then continuously decreases up to 140 m, and then increases again up to the bottom of the CBL. Finally, it ( $\bar{w}'e$ ) sharply decreases to null at the CBL top (Figures 10e–10f).

In the case of SCPM-M with higher amplitudes, the changes are more abrupt within the CBL and it approaches zero slightly above and below the CBL height (Figure 10e). Also, at higher amplitudes, their profiles are not exactly the same but are slightly different throughout the boundary layer up to the CBL top (Figure 10e). However, at the lower and medium amplitude SCPM-M cases, the turbulent transport terms are almost similar to the No-SCPM case above 200 m (Figure 10f). Similar to the higher amplitude SCPM-M cases,  $\bar{w}'e$  reaches zero slightly above and below the CBL height (Figure 10f) for the lower and medium amplitude SCPM-M cases.

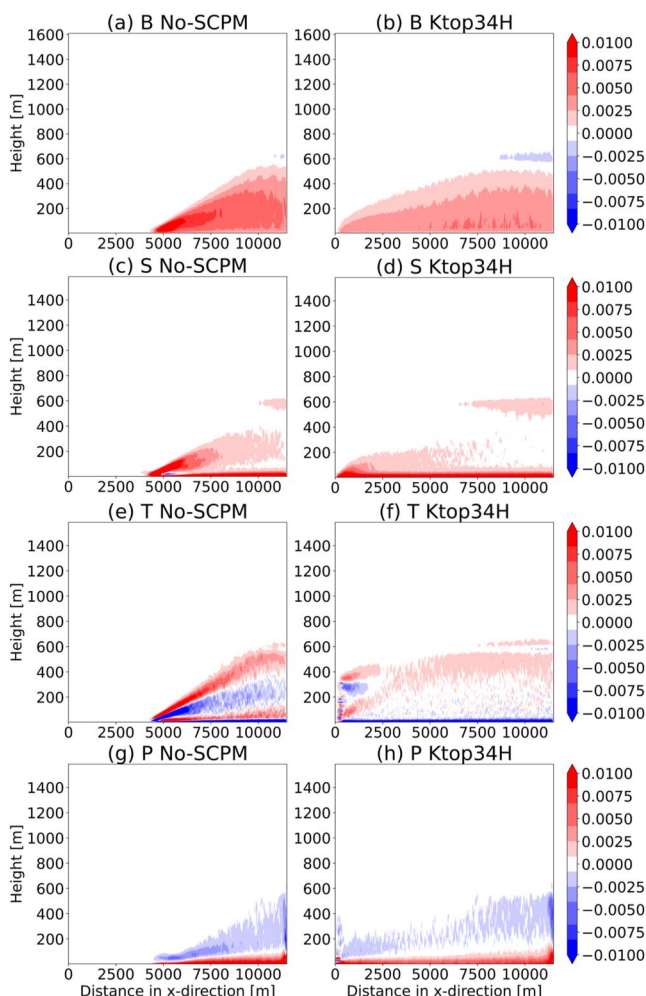


**Figure 9.**  $Y$ -averaged turbulent kinetic energy (TKE) budget terms after applying momentum perturbation following (Table 1), for the buoyancy term with (a) No-SCPM, (b) Ktop34H, for the shear production term with (c) No-SCPM (d) Ktop34H, for the turbulent transport with (e) No-SCPM (f) Ktop34H, and for the pressure correlation term with (g) No-SCPM, (h) Ktop34H. The color bar corresponds to the magnitude of TKE budget terms for panels (a–h). These plots are generated for TKE budget terms that are  $Y$ -averaged over the entire inner domain.

## 4. Conclusions

In this work, we studied the impact of momentum perturbations, employed to generate turbulence in boundary-coupled LES simulations, on the TKE budget terms in an unstable boundary layer. It is well known that LES models that are used with periodic boundary conditions are capable of representing fully developed turbulence. However, turbulence representation is challenging in models that couple mesoscale and microscale domains or when conducting LES simulations with non-periodic conditions, such as in the presence of complex topography. Additional turbulence-generation techniques are needed in these instances. Several such techniques have been developed in the past, each one with its own advantages and disadvantages. Here, we implemented the stochastic cell perturbation technique in WRF-LES simulations to study the impact of turbulence generation on the TKE

### 3.4.4. Pressure Correlation Term

The pressure correlation term plays the role of redistributing TKE within the boundary layer. Additionally, in some cases, the pressure covariance does not dissipate energy but transfers it out of the boundary layer through gravity waves (Stull, 1988). Applying SCPM-M significantly reduces the fetch in the redistribution of TKE through the pressure correlation term, and the area-averaged profiles become smoother, as shown in Figure 10g and Figures S6a–S6f in Supporting Information S1. The redistribution of TKE starts from the beginning of the domain with higher and medium amplitude perturbations, while it starts after  $x = 100$  m for the lower amplitude SCPM-M cases (Figure 9h and Figures S6a–S6f in Supporting Information S1). In the case of Ktop54H and Ktop88H, we observe some spurious motions at the beginning of the domain (at the inflow boundary), as shown in Figures S6a and S6b of Supporting Information S1.

We observe that applying momentum perturbation results in a higher magnitude of pressure correlation terms as compared to the No-SCPM case (Figures 10g and 10h). The magnitudes of these terms are slightly higher in the case of SCPM-M with higher amplitudes as compared to the SCPM-M cases with lower amplitudes (Figures 10g and 10h). The differences among higher and lower amplitude SCPM-M cases are not significant below 100 m as there are very low magnitudes of pressure fluctuations in the surface layer (i.e., the lowest 10% of the boundary layer).

### 3.4.5. Temporal Evolution of TKE

In this subsection, we investigate the evolution of the TKE with time to examine how long the effect of the momentum perturbation lasts after the perturbations are turned off. And then, if we want to maintain the sustained turbulence in the atmosphere, how frequently should we add these perturbations? We would like to clarify that it is neither about the lingering effects of perturbations nor about the application of perturbation during day and night. The SCPM-M simulations are performed for two hours, starting from 18 Z (UTC) to 20 Z (UTC). The application of external forces creates inertia, which is present for the next half an hour from the time when the momentum perturbation is stopped. As shown in Figure 11, although the magnitude of TKE that is generated due to inertia is low, it still remains finite from 20 to 20:30 Z in the two cases, that is, Ktop54H and Ktop88H (Figures 11a and 11c) (Ktop34H is not shown here but similar results are expected). Comparing the results after 20:30 Z (Figures 11a and 11c; Figures 11b and 11d), it is clear that the TKE dissipates and the effect of inertia is no longer present after 20:30 Z (UTC).

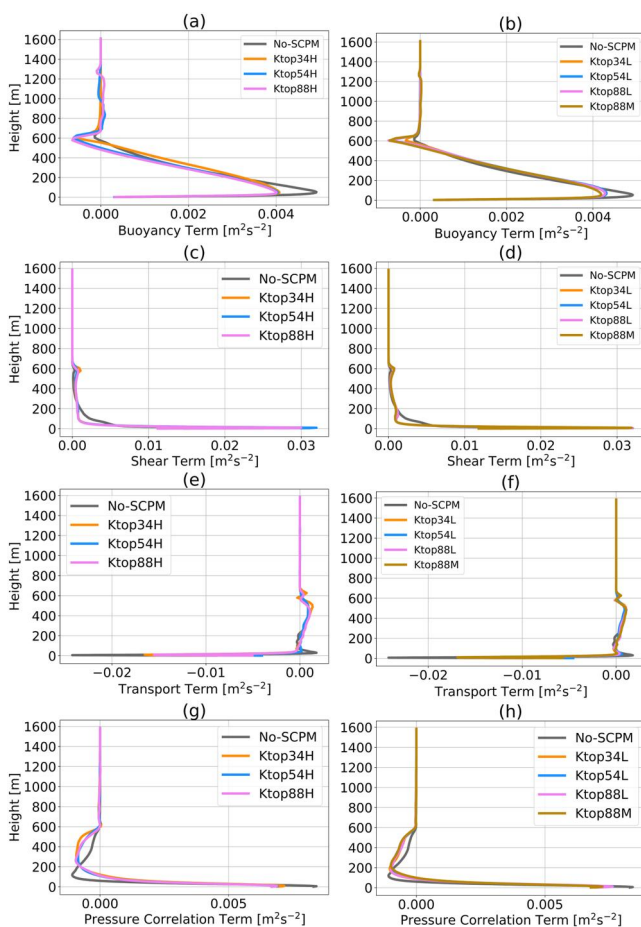


**Figure 10.** Area-averaged turbulent kinetic energy budget terms over the last three-quarters of the domain, that is, overall  $y$  and  $x$  from 2,880 to 11,520 m after applying momentum perturbation for the buoyancy term with (a) higher amplitudes, (b) lower and medium amplitudes; for the shear production term with (c) higher amplitudes (d) lower and medium amplitudes; for the turbulent transport with (e) higher amplitudes (f) lower and medium amplitudes; and for the pressure correlation term with (g) higher amplitudes, (h) lower and medium amplitudes. These plots are shown for the top of the inner domain from the simulation (up to 1,608 m).

boundary layer or between the CBL height and the surface layer reduces additional entrainment-induced motions and computational costs. Based on the cases studied here, it can be concluded that applying momentum perturbations up to half the CBL height (the Ktop34H case) is optimal. This is because the Ktop34H case was characterized by significant fetch reduction and minimum generation of additional turbulent motions at the inversion layer.

The application of momentum perturbations to generate turbulence in boundary-coupled LES simulations can benefit a number of disciplines and applications, including but not limited to wind energy generation, wildfire modeling, cloud top boundary layer research (applicable to off-shore wind), and dispersion problems. Accurate turbulence representation is also important for Uncrewed Aerial Vehicle research and weather forecasting. The results of this work will benefit these applications leading to an improved understanding of the physical Earth system models.

budget. We used an LES domain with a horizontal resolution of 12 m, which was nested within a mesoscale domain with a horizontal resolution of 240 m. Momentum perturbations were applied in the horizontal and vertical directions at the inflow boundaries of the LES domain. We performed experiments where we varied perturbation amplitudes, as well as the heights to which the perturbations were applied with respect to the CBL height.

Applying SCPM-M accelerated turbulence generation, and significantly reduced the fetch, for all cases studied. Fetch reduction in coupled mesoscale-microscale atmospheric simulations results in lower computational costs of numerical experiments since a smaller domain would need to be resolved. While the magnitude of TKE produced was always higher for the SCPM-M cases than the No-SCPM case, we found that turbulence strength depended on the amplitude of perturbations, with higher-amplitude perturbations producing more turbulence than medium and lower-amplitude perturbations. Simulations with perturbations produced larger variances in the velocities up to the inversion layer than the No-SCPM simulation. This also contributed to higher heat and momentum fluxes. We found that SCPM-M simulations provided comparable results with observations and that the model outputs are consistent with it. In summary, atmospheric stability plays a critical role in the generation and evolution of turbulence in the boundary layer. Stable atmospheric conditions suppress turbulence generation, while unstable conditions enhance it.

The perturbations also affected buoyancy production. SCPM-M simulations produced slightly more buoyancy than the No-SCPM case in the bottom and top third of the boundary layer, while buoyancy in the SCPM-M simulations was comparable to that in the No-SCPM case in the middle third of the boundary layer. Shear production for the SCPM-M cases was higher than that for the No-SCPM case near the surface up to 35 m. Beyond this height, it decreased until it attained a value equal to the No-SCPM case at 200 m. Near the inversion layer, the shear production term in the SCPM-M case increased again due to entrainment-induced motions. The implementation of perturbations also impacted TKE redistribution through turbulent transport and pressure correlation terms. Our findings suggest that momentum perturbation enhances the coupling between shear and buoyancy-driven turbulence under unstable conditions.

Applying perturbations above the CBL height generated spurious turbulent structures attributed to additional entrainment at the top of the boundary layer, near the inversion layer. On the other hand, applying SCPM-M within the

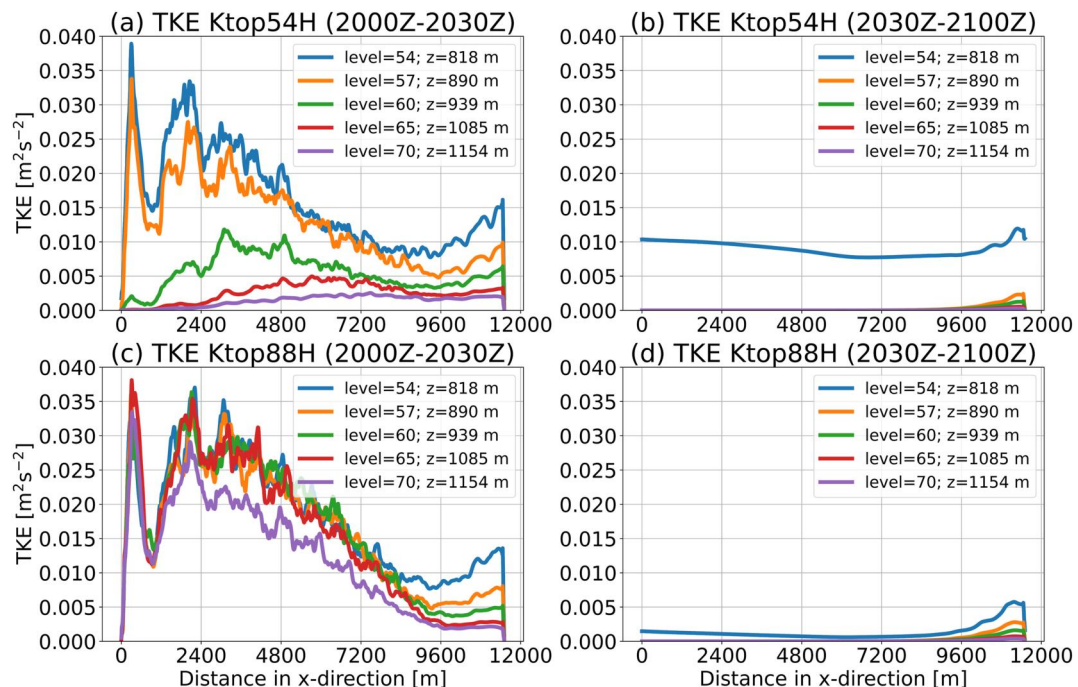


**Figure 11.** Y and time-averaged turbulent kinetic energy ( $\text{m}^2/\text{s}^2$ ) profiles, computed at different heights in the atmosphere during an unstable case when momentum perturbation was turned off from (a) 20 Z to 20:30 Z (UTC) for Ktop54H, (b) 20:30–21:00 Z (UTC) for Ktop54H, (c) 20–20:30 Z (UTC) for Ktop88H, and (d) 20:30–21:00 Z (UTC) for Ktop88H in the different panels of the figure. These profiles are generated for buoyancy terms that are area-averaged over the entire inner domain.

## Acknowledgments

Funding for this work was provided by the U.S. DOE Office of Energy Efficiency and Renewable Energy Wind Energy Technologies Office. M. Kumar acknowledges funding support from the Dean's Dissertation Fellowship award from the Henry Samueli School of Engineering at the University of California Irvine, and the Research Applications Laboratory visitor grant from the National Center for Atmospheric Research (NCAR). M. Kumar and T. Banerjee acknowledge support from the Subcontract agreement with Los Alamos National Laboratory, subcontract no. 596883, agreement no. 351438. Banerjee is supported by the US National Science Foundation (NSF-AGS-PDM-2146520, NSF-OISE-2114740, NSF-CPS-2209695, NSF-ECO-CBET-2318718, and NSF-DMS-2335847), the University of California Office of the President (UCOP-LFR-20-653572), NASA (80NSSC22K1911), and the United States Department of Agriculture (NIFA 2021-67022-35908, and USDA-20-CR-11242306-072). The contribution of Branko Kosović was supported by the NCAR, which is a major facility sponsored by the National Science Foundation under Cooperative Agreement No. 1852977. William Lassman's and Jeffrey D. Mirocha's contributions were performed under the auspices of the U.S. Department of Energy by Lawrence Livermore National Laboratory under Contract DE-AC52-07NA27344. This research used resources provided by the Los Alamos National Laboratory Institutional Computing Program, which is supported by the U.S. Department of Energy National Nuclear Security Administration under Contract DE-AC52-06NA25396.

## Conflict of Interest

The authors declare no conflicts of interest relevant to this study.

## Data Availability Statement

The simulations used in this study are performed using the latest release of the WRF (v4.1.3) model (<https://github.com/wrf-model/WRF>). The data sets produced or analyzed in the present study can be obtained upon reasonable request from the corresponding author.

## References

Ching, J., Rotunno, R., LeMone, M., Martilli, A., Kosovic, B., Jimenez, P., & Dudhia, J. (2014). Convectively induced secondary circulations in fine-grid mesoscale numerical weather prediction models. *Monthly Weather Review*, 142(9), 3284–3302. <https://doi.org/10.1175/mwr-d-13-00318.1>

Connolly, A., van Veen, L., Neher, J., Geurts, B. J., Mirocha, J., & Chow, F. K. (2021). Efficacy of the cell perturbation method in large-eddy simulations of boundary layer flow over complex terrain. *Atmosphere*, 12(1), 55. <https://doi.org/10.3390/atmos12010055>

Deardorff, J. W. (1972). Numerical investigation of neutral and unstable planetary boundary layers. *Journal of the Atmospheric Sciences*, 29(1), 91–115. [https://doi.org/10.1175/1520-0469\(1972\)029<0091:nionau>2.0.co;2](https://doi.org/10.1175/1520-0469(1972)029<0091:nionau>2.0.co;2)

Deardorff, J. W. (1980). Stratocumulus-capped mixed layers derived from a three-dimensional model. *Boundary-Layer Meteorology*, 18(4), 495–527. <https://doi.org/10.1007/bf00119502>

Di Mare, L., Klein, M., Jones, W., & Janicka, J. (2006). Synthetic turbulence inflow conditions for large-eddy simulation. *Physics of Fluids*, 18(2), 025107. <https://doi.org/10.1063/1.2130744>

dos Santos, I. D.-R., & Yaghoobian, N. (2023). Effects of urban boundary layer turbulence on firebrand transport. *Fire Safety Journal*, 135, 103726. <https://doi.org/10.1016/j.firesaf.2022.103726>

Giani, P., Genton, M. G., & Crippa, P. (2022). Modeling the convective boundary layer in the terra incognita: Evaluation of different strategies with real-case simulations. *Monthly Weather Review*, 150(5), 981–1001. <https://doi.org/10.1175/mwr-d-21-0216.1>

Haupt, S. E., Arthur, R., Decastro, A., Gagne, D. J., Jonko, A., Kosovic, B., et al. (2020). *FY2020 report of the atmosphere to electrons land-based mesoscale-to-microscale coupling project* (Technical report). Pacific Northwest National Laboratory (PNNL).

Haupt, S. E., Berg, L. K., Decastro, A., Gagne, D. J., Jimenez, P., Juliano, T., et al. (2019). *FY 2019 report of the atmosphere to electrons mesoscale-to-microscale coupling project* (Technical report). Pacific Northwest National Laboratory (PNNL).

Haupt, S. E., Kosovic, B., Shaw, W., Berg, L. K., Churchfield, M., Cline, J., et al. (2019). On bridging a modeling scale gap: Mesoscale to microscale coupling for wind energy. *Bulletin of the American Meteorological Society*, 100(12), 2533–2550. <https://doi.org/10.1175/bams-d-18-0033.1>

Hong, S.-Y., Noh, Y., & Dudhia, J. (2006). A new vertical diffusion package with an explicit treatment of entrainment processes. *Monthly Weather Review*, 134(9), 2318–2341. <https://doi.org/10.1175/mwr3199.1>

Jähn, M., Muñoz-Esparza, D., Chouza, F., Reitebuch, O., Knoth, O., Haarig, M., & Ansmann, A. (2016). Investigations of boundary layer structure, cloud characteristics and vertical mixing of aerosols at Barbados with large eddy simulations. *Atmospheric Chemistry and Physics*, 16(2), 651–674. <https://doi.org/10.5194/acp-16-651-2016>

Jiménez, P. A., Dudhia, J., González-Rouco, J. F., Navarro, J., Montávez, J. P., & García-Bustamante, E. (2012). A revised scheme for the WRF surface layer formulation. *Monthly Weather Review*, 140(3), 898–918. <https://doi.org/10.1175/mwr-d-11-00056.1>

Keat, A., Piomelli, U., Ballaras, E., & Kaltenbach, H. (2004). A priori and a posteriori tests of inflow conditions for large-eddy simulations. *Physics of Fluids*, 16, 4696–4712.

Klein, M., Sadiki, A., & Janicka, J. (2003). A digital filter based generation of inflow data for spatially developing direct numerical or large eddy simulations. *Journal of Computational Physics*, 186(2), 652–665. [https://doi.org/10.1016/s0021-9991\(03\)00090-1](https://doi.org/10.1016/s0021-9991(03)00090-1)

Kosović, B. (1997). Subgrid-scale modelling for the large-eddy simulation of high-Reynolds-number boundary layers. *Journal of Fluid Mechanics*, 336, 151–182. <https://doi.org/10.1017/s0022112096004697>

Kumar, M. (2022). *Mapping and modeling of fires in the wildland-urban interface*. University of California, Irvine.

Kumar, M., Banerjee, T., Jonko, A., Mirocha, J., & Lassman, W. (2021). Assessing the turbulence kinetic energy budget in the boundary layer using WRF-les: Impact of momentum perturbation. In *EGU General Assembly Conference Abstracts* (p. EGU21-13794).

Kumar, M., Frediani, M., Juliano, T. W., Kosovic, B., Randerson, J. T., & Banerjee, T. (2022). The role of fire-induced turbulence on ember transport. In *AGU Fall Meeting Abstracts* (Vol. 2022, p. A25F–1784).

Kumar, M., Kosovic, B., Nayak, H., Porter, W., Randerson, J., & Banerjee, T. (2024). Evaluating the performance of WRF in simulating winds and surface meteorology during a Southern California wildfire event. *Frontiers in Earth Science*, 11, 1305124. <https://doi.org/10.3389/feart.2023.1305124>

Le, H., Moin, P., & Kim, J. (1997). Direct numerical simulation of turbulent flow over a backward-facing step. *Journal of Fluid Mechanics*, 330, 349–374. <https://doi.org/10.1017/s0022112096003941>

Liu, Y., Warner, T., Liu, Y., Vincent, C., Wu, W., Mahoney, B., et al. (2011). Simultaneous nested modeling from the synoptic scale to the les scale for wind energy applications. *Journal of Wind Engineering and Industrial Aerodynamics*, 99(4), 308–319. <https://doi.org/10.1016/j.jweia.2011.01.013>

Mazzaro, L., Koo, E., Muñoz-Esparza, D., Lundquist, J., & Linn, R. (2019). Random force perturbations: A new extension of the cell perturbation method for turbulence generation in multiscale atmospheric boundary layer simulations. *Journal of Advances in Modeling Earth Systems*, 11(7), 2311–2329. <https://doi.org/10.1029/2019ms001608>

Mazzaro, L. J., Muñoz-Esparza, D., Lundquist, J. K., & Linn, R. R. (2017). Nested mesoscale-to-LES modeling of the atmospheric boundary layer in the presence of under-resolved convective structures. *Journal of Advances in Modeling Earth Systems*, 9(4), 1795–1810. <https://doi.org/10.1002/2017ms000912>

Mirocha, J., Kosović, B., & Kirkil, G. (2014). Resolved turbulence characteristics in large-eddy simulations nested within mesoscale simulations using the weather research and forecasting model. *Monthly Weather Review*, 142(2), 806–831. <https://doi.org/10.1175/mwr-d-13-00064.1>

Mirocha, J., Lundquist, J., & Kosović, B. (2010). Implementation of a nonlinear subfilter turbulence stress model for large-eddy simulation in the advanced research WRF model. *Monthly Weather Review*, 138(11), 4212–4228. <https://doi.org/10.1175/2010mwr3286.1>

Moeng, C.-H., & Sullivan, P. P. (1994). A comparison of shear-and buoyancy-driven planetary boundary layer flows. *Journal of the Atmospheric Sciences*, 51(7), 999–1022. [https://doi.org/10.1175/1520-0469\(1994\)051<0999:acosab>2.0.co;2](https://doi.org/10.1175/1520-0469(1994)051<0999:acosab>2.0.co;2)

Moeng, C.-H., & Wyngaard, J. C. (1984). Statistics of conservative scalars in the convective boundary layer. *Journal of the Atmospheric Sciences*, 41(21), 3161–3169. [https://doi.org/10.1175/1520-0469\(1984\)041<3161:socsl>2.0.co;2](https://doi.org/10.1175/1520-0469(1984)041<3161:socsl>2.0.co;2)

Monin, A. S., & Obukhov, A. M. (1954). Basic laws of turbulent mixing in the surface layer of the atmosphere. *Contributions of the Geophysical Institute of the Academy of Sciences USSR*, 15(163), e187.

Muñoz-Esparza, D., & Kosović, B. (2018). Generation of inflow turbulence in large-eddy simulations of nonneutral atmospheric boundary layers with the cell perturbation method. *Monthly Weather Review*, 146(6), 1889–1909. <https://doi.org/10.1175/mwr-d-18-0077.1>

Muñoz-Esparza, D., Kosović, B., García-Sánchez, C., & van Beeck, J. (2014). Nesting turbulence in an offshore convective boundary layer using large-eddy simulations. *Boundary-Layer Meteorology*, 151(3), 453–478. <https://doi.org/10.1007/s10546-014-9911-9>

Muñoz-Esparza, D., Kosović, B., Mirocha, J., & van Beeck, J. (2014). Bridging the transition from mesoscale to microscale turbulence in numerical weather prediction models. *Boundary-Layer Meteorology*, 153(3), 409–440. <https://doi.org/10.1007/s10546-014-9956-9>

Muñoz-Esparza, D., Kosović, B., van Beeck, J., & Mirocha, J. (2015). A stochastic perturbation method to generate inflow turbulence in large-eddy simulation models: Application to neutrally stratified atmospheric boundary layers. *Physics of Fluids*, 27(3), 035102. <https://doi.org/10.1063/1.4913572>

Muñoz-Esparza, D., Lundquist, J. K., Sauer, J. A., Kosović, B., & Linn, R. R. (2017). Coupled mesoscale-LES modeling of a diurnal cycle during the CWEX-13 field campaign: From weather to boundary-layer eddies. *Journal of Advances in Modeling Earth Systems*, 9(3), 1572–1594. <https://doi.org/10.1002/2017ms000960>

Muñoz-Esparza, D., Sauer, J. A., Linn, R. R., & Kosović, B. (2016). Limitations of one-dimensional mesoscale PBL parameterizations in reproducing mountain-wave flows. *Journal of the Atmospheric Sciences*, 73(7), 2603–2614. <https://doi.org/10.1175/jas-d-15-0304.1>

Pamies, M., Weiss, P.-E., Garnier, E., Deck, S., & Sagaut, P. (2009). Generation of synthetic turbulent inflow data for large eddy simulation of spatially evolving wall-bounded flows. *Physics of Fluids*, 21(4), 045103. <https://doi.org/10.1063/1.3103881>

Rai, R. K., Berg, L. K., Kosović, B., Mirocha, J. D., Pekour, M. S., & Shaw, W. J. (2017). Comparison of measured and numerically simulated turbulence statistics in a convective boundary layer over complex terrain. *Boundary-Layer Meteorology*, 163(1), 69–89. <https://doi.org/10.1007/s10546-016-0217-y>

Rai, R. K., Berg, L. K., Pekour, M., Shaw, W. J., Kosovic, B., Mirocha, J. D., & Ennis, B. L. (2017). Spatiotemporal variability of turbulence kinetic energy budgets in the convective boundary layer over both simple and complex terrain. *Journal of Applied Meteorology and Climatology*, 56(12), 3285–3302. <https://doi.org/10.1175/jamc-d-17-0124.1>

Sauer, J. A., Muñoz-Esparza, D., Canfield, J. M., Costigan, K. R., Linn, R. R., & Kim, Y.-J. (2016). A large-eddy simulation study of atmospheric boundary layer influence on stratified flows over terrain. *Journal of the Atmospheric Sciences*, 73(7), 2615–2632. <https://doi.org/10.1175/jas-d-15-0282.1>

Skamarock, W. C., Klemp, J. B., Dudhia, J., Gill, D. O., Liu, Z., Berner, J., et al. (2019). *A description of the advanced research WRF model version 4* (Vol. 145). National Center for Atmospheric Research.

Smith, C. M., & Skillingstad, E. D. (2009). Investigation of upstream boundary layer influence on mountain wave breaking and lee wave rotors using a large-eddy simulation. *Journal of the Atmospheric Sciences*, 66(10), 3147–3164. <https://doi.org/10.1175/2009jas2949.1>

Spille-Kohoff, A., & Kaltenbach, H.-J. (2001). *Generation of turbulent inflow data with a prescribed shear-stress profile* (Technical report). Technische University Berlin (Germany) Hermann-Fottinger Inst fur Stromungsmechanik.

Stull, R. B. (1988). *An introduction to boundary layer meteorology* (Vol. 13). Springer Science & Business Media.

Tabor, G. R., & Baba-Ahmadi, M. (2010). Inlet conditions for large eddy simulation: A review. *Computers & Fluids*, 39(4), 553–567. <https://doi.org/10.1016/j.compfluid.2009.10.007>

Talbot, C., Bou-Zeid, E., & Smith, J. (2012). Nested mesoscale large-eddy simulations with WRF: Performance in real test cases. *Journal of Hydrometeorology*, 13(5), 1421–1441. <https://doi.org/10.1175/jhm-d-11-048.1>

Xie, Z.-T., & Castro, I. P. (2008). Efficient generation of inflow conditions for large eddy simulation of street-scale flows. *Flow, Turbulence and Combustion*, 81(3), 449–470. <https://doi.org/10.1007/s10494-008-9151-5>

Zajaczkowski, F. J., Haupt, S. E., & Schmehl, K. J. (2011). A preliminary study of assimilating numerical weather prediction data into computational fluid dynamics models for wind prediction. *Journal of Wind Engineering and Industrial Aerodynamics*, 99(4), 320–329. <https://doi.org/10.1016/j.jweia.2011.01.023>

Zhong, J., Cai, X., & Xie, Z.-T. (2021). Implementation of a synthetic inflow turbulence generator in idealised WRF v3. 6.1 large eddy simulations under neutral atmospheric conditions. *Geoscientific Model Development*, 14(1), 323–336. <https://doi.org/10.5194/gmd-14-323-2021>

Zhou, B., & Chow, F. K. (2013). Nighttime turbulent events in a steep valley: A nested large-eddy simulation study. *Journal of the Atmospheric Sciences*, 70(10), 3262–3276. <https://doi.org/10.1175/jas-d-13-02.1>